In vivo multiscale measurements of solid stresses in tumors reveal scale-dependent stress transmission

Sue Zhang
Boston University
Rachel Passaro
Boston University
Kathryn Regan
Boston University
Muhamed Hadzipasic
Boston University, Massachusetts General Hospital
Gabrielle Grifno
Boston University
Siyi Zheng
Boston University https://orcid.org/0000-0001-5514-2768
Logan O'Connor
Boston University
Vinson Chu
Boston University
Sung Yeon Kim
Boston University
Jiarui Yang
Rohin Banerji
Boston University
Kavon Karrobi
Boston University
Darren Roblyer
Boston University https://orcid.org/0000-0002-5301-4364
Mark Grinstaff
Boston University https://orcid.org/0000-0002-5453-3668
Hadi Nia (htnia@bu.edu)
Boston University https://orcid.org/0000-0003-1970-9901

Article

Keywords:

Posted Date: June 13th, 2022

DOI: https://doi.org/10.21203/rs.3.rs-1697924/v1

In vivo multiscale measurements of solid stresses in tumors reveal scale-dependent stress transmission

Sue Zhang[1], Rachel Passaro[1], Kathryn Regan[1], Muhamed Hadzipasic[1,3], Gabrielle Grifno[1], Siyi Zheng[1], Logan O'Connor[1], Vinson Chu[1], Sung Yeon Kim[1], Jiarui Yang[1], Rohin Banerji[1], Kavon Karrobi[1], Darren Roblyer[1], Mark Grinstaff[1,2], Hadi T. Nia[1,*]

[1]Department of Biomedical Engineering, Boston University, Boston, MA
[2]Department of Chemistry, Boston University, Boston, MA
[3]Department of Neurosurgery, Massachusetts General Hospital, Boston, MA
*: Corresponding author

Abstract:

Solid stress, one of the physical hallmarks of cancer, affects trafficking and infiltration of immune cells, promotes metastasis and tumorigenic pathways, and impedes therapeutic delivery. Despite these clinical ramifications, questions remain regarding the origins and consequences of solid stresses and the differential response of tumor versus normal cells to solid stresses. Answering these fundamental questions requires probing solid stresses at the cellular scale, where biological and immunological responses manifest, as well as *in vivo*, where the complexities of the tumor microenvironment are present. Here, we report the first *in vivo* and multi-scale measurements of solid stress in mouse models of breast cancer using multi-modal intravital microscopy of deformable hydrogels complemented with mathematical modeling. Utilizing the capabilities of these methods, such as the high-resolution, longitudinal, and 3-D measurements of local solid stress, we measure and compare solid stresses (i) at the single cell vs tissue scale, (ii) primary vs metastatic tumors, (iii) *in vivo* vs *in vitro* settings, and (iv) *in vivo* vs post-mortem. Surprisingly, we find solid stress transmission is scale-dependent, as tumor cells experience a factor of 6 reduction in stress in comparison to stress measured at the tissue scale. This finding implicates the presence of potential biophysical mechanisms that tumor cells utilize to protect themselves against lethally high solid stresses. This insight into the scale-dependence of solid stress genesis will further inform the discovery of new therapeutic strategies that sensitize cancer cells to solid stresses to induce cell death.

Introduction

Solid stress, defined as the mechanical force generated and transmitted by the solid components of a tumor, is a newly identified physical hallmark of cancer with crucial consequences for tumor progression and treatment response[1]. Cells sense solid stresses directly and indirectly via mechanosensitive interactions such as cell-extracellular matrix (ECM) and cell-cell adhesions[2–5], activation of tensile-responsive ECM proteins[6–8], and nuclear deformation[9,10]. Solid stress causes the compression of blood and lymphatic vessels[1,11–13] which contributes to hypoxia[11,13] and impedes drug delivery[14,15], affects T-cell trafficking and infiltration[16], promotes invasiveness of cancer cells[17,18], stimulates tumorigenic pathways[19], and induces neuronal damage[20,21]. Targeting solid stress, when combined with standard-of-care anti-cancer treatments, prolongs survival in preclinical studies[11,22,23] and is currently being evaluated in clinical trials[24] with promising outcomes[25]. While some of the pathophysiological consequences of solid stresses in tumors are now better known, the direct cellular responses to solid stresses and the molecular pathways that are directly activated by them are not fully understood. This is due mainly to a lack of appropriate tools to measure the solid stresses that individual single cancer cells experience *in vivo*, where the complexities of tumor microenvironment are present.

Despite the recent progress in measuring solid stresses *ex vivo*[20,21,26,27] and *in vitro*[28–31], *in vivo* measurement of solid stress in tumors is an unmet need. An *in vivo* measurement of solid stress with high spatiotemporal resolution would allow deeper insight into the origins and consequences of solid stresses. In addition, the existing methods to measure solid stresses in murine and human tumors[20,21,26,27] are at the tissue scale and lack the spatial resolution to measure the stresses that individual tumor cells experience. These existing methods are also invasive, typically performed at terminal points, and lack the capabilities for longitudinal monitoring of solid stresses. Furthermore, the existing methods are limited to reporting 1-D and 2-D profiles of solid stresses[26,27] and do not provide the 3-D distribution of solid stress as a tensor, which is necessary to describe the anisotropy and heterogeneities of stresses. Therefore, it is critical to develop a method to non-invasively monitor *in vivo* solid stresses at high spatiotemporal resolution across the length scales from the cellular to the tissue scale.

Our previous methods showed that solid stresses measured at the macroscale in tumors result in up to 20% strain (deformation) after partial stress relaxation[26,27], reflecting extremely high stresses in the tumors that are lethal to cells[32,33,34] and in the normal surrounding tissue[20]. These observations raised the following open questions that motivate our current study to measure solid stresses at the cellular level: How can tumor cells survive under such high solid stresses? Are there any biological and/or physical mechanisms that tumor cells utilize to protect themselves from lethally high solid stresses? Recently proposed biological mechanisms to protect tumor cells against high levels of solid stress include the loss of p53 to enable neoplastic cells to survive under high mechanical stress[5,34]. However, such biological mechanisms only protect cells with loss of p53 function, and do not explain how other cancer and stromal cells in the tumor are protected against solid stresses. In this study, we show that, in addition to biological mechanisms, potential biophysical mechanisms may dissipate the large tissue-level stresses and protect tumor cells against high level of solid stresses.

Here, we describe the first *in vivo* and multi-scale measurements of solid stress using different intravital microscopy modalities in a mouse model of primary breast cancer and lung metastasis. Our method enables multi-scale measurements to investigate differences in solid stress at the cellular vs tissue scales and allows for 3-D high-resolution and longitudinal measurement of solid stresses *in vivo*. Furthermore, our method enables the comparison between the *in vitro* and *in vivo* models of solid stresses to evaluate how closely these *in vitro* models recapitulate the physical tumor microenvironment. Our multiscale method for measuring *in vivo* solid stresses reveals, for the first time, that solid stress transmission is scale dependent. Unexpectedly, we find that the stresses that individual tumor cells experience is a factor of 6 lower than the large stress levels measured at the tissue scales. This finding lays the groundwork for discovering novel biophysical mechanisms that cancer cells utilize to evade cell death from high mechanical stresses, and for establishing new therapeutic strategies aimed at increasing the vulnerability of cancer cells to mechanical stresses, resulting in cancer cell death.

Results

Development of an *in vivo* solid stress measurement system for primary and metastatic tumors

To measure solid stress *in vivo*, we employed intravital imaging of spherical polyacrylamide (PA) beads as solid stress sensors. PA beads are biocompatible, deformable, tunable in size and Young's modulus, and amenable to core and surface functionalization, including covalent attachment of a fluorophore[31]. We fabricated PA beads using an inverse emulsion polymerization, as previously reported[28,29,35] and filtered them for the desired size ranges using micron-sized meshes. After sterilization by UV light, PA beads were functionalized with fibronectin to mimic cell-matrix interactions between the

PA beads and surrounding tissue and to promote uptake of PA beads into murine tumors (Fig. 1a). PA beads were fabricated for measurements at the tissue-scale (397 ± 69 μm in diameter) or cellular-scale (28.7 ± 18.2 μm) to investigate the scale-dependence of solid stress across an order of magnitude change in length scale (Fig. 1b). Implementing a syngeneic model of breast cancer, MCa-M3C cancer cells[36], transduced with H2B-dendra2, were co-injected orthotopically with PA beads into the mammary fat pad of FVB mice for primary mammary tumors or tail-vein for metastatic lung tumors (Fig. 1c). Custom-designed, 3D-printed intravital mammary windows (Fig. S1) were used in intravital imaging to allow visualization of PA beads and cancer cells via different modes of optical microscopy. For *in vitro* experiments, MCa-M3C-H2B-dendra2 cancer cells and PA beads were mixed to form spheroid models (Fig. 1c). Based on the length-scale of the bead and imaging depth requirements, imaging modalities with appropriate spatial resolutions and depth penetrations were used to image the beads embedded within tumors (Fig. 1d): Confocal microscopy was used to image the cellular-scale beads (28.7 ± 18.2 μm) in *in vitro* spheroids, two-photon microscopy (2P) was used to image *in vivo* cellular-scale beads (28.7 ± 18.2 μm), and optical coherence tomography (OCT) was used to image *in vivo* tissue-scale beads (397 ± 69 μm) (Fig. 1d). To examine whether the presence of the PA beads affects the tumor microenvironment, we performed hematoxylin and eosin (H&E) staining of tumor slices and observed no distinct fibrosis or inflammation around the PA bead compared to regions far from the bead (Fig. 1e). Our method allowed longitudinal monitoring of cellular-scale and tissue-scale stresses up to 7 and 14 days, respectively (Fig. S2). Tumor growth and fibrosis occurring in response to window implantation caused beads to become out of view and limited the length of time allowed for longitudinal imaging. Due to the high penetration depth of ~2mm for OCT, the number of days in which beads could still be visualized was longer for the tissue scale.

To accurately quantify solid stresses in a wide dynamic range, it was critical to tune the Young's modulus of PA beads to a level that they will deform in response to the intratumoral solid stress. If the PA beads were too stiff (Fig. 1f (i-iii)), the resulting deformation will be small and unreliable for quantifying solid stress in the tumor, and if the beads were too soft, they may break or plastically deform in response to solid stress in tumors. We used atomic force microscopy (AFM) to measure the Young's modulus of the beads (Fig. 1g), and optimized the Young's moduli of PA beads through multiple *in vitro* and *in vivo* trials. We found that PA beads with Young's moduli of E=0.21 ± 0.04 kPa and E=0.38± 0.15 kPa resulted in large enough deformations to be detected at the cellular scale and tissue scale, respectively, and can thus detect solid stress levels more sensitively than PA beads with higher Young's moduli (Fig. 1f (iv-vi)). Furthermore, the optimized stiffness values of the PA beads were in the same order of magnitude as cells, spheroids, and tumors and therefore can be appropriately used to estimate the stress experienced by cells (Fig. 1h).

We analyzed the deformation in PA beads by determining the absolute value of the principal solid stress tensor in Pascals and elastic energy density in J/m^3 using a 3-D finite element model (FEM) developed in the commercial software ABAQUS (Fig. 1i(iv)). The solid stress distribution and elastic energy density were estimated by applying the appropriate boundary condition that deforms an originally spherical bead to the geometry obtained through intravital imaging of the PA beads (Fig. 1i(ii,iii)). We accounted for nonlinear behavior of polyacrylamide under large deformations by directly measuring the nonlinear, hyperelastic properties of the hydrogel (Fig. S3). For the large deformations we observed, using nonlinear elastic properties is essential as we showed that using a nonlinear model results in solid stress values that are 2x higher compared to using a linear model (Fig. S4). Furthermore, we experimentally

determined the Poisson's ratio of polyacrylamide to be 0.22 ± 0.03 by measuring the axial and lateral strain resulting from compressing a bulk polyacrylamide gel. Our parametric study showed that the Poisson's ratio of 0.22 results in stress response close to a compressible material (Fig. S5). For the beads which were embedded in tissues that were not enzymatically dissociated and, therefore, had undeformed diameters that could not be measured exactly, the diameter of the original spherical bead was assumed to be the largest axis length of the deformed bead as a reasonable approximation based on comparisons between the deformed and undeformed diameters of PA beads (Fig. S6).

Additionally, and to make this estimation accessible to users without knowledge of or access to finite element modeling, we reported the aspect ratio of the beads from their 3-D geometry obtained via intravital imaging (Fig. 1i(i)): given a known and consistent Young's modulus of the beads, we inferred a higher anisotropic solid stress in the deformed beads with higher aspect ratio. While the aspect ratio of the beads cannot reflect the isotopic stresses, this method provided a simple and relative estimate of the anisotropic stress magnitude and direction. After segmenting the bead in the 3-D image stacks, each bead was approximated to an ellipsoid[37] and the three axis length values were obtained (Fig. 1i(i)). The aspect ratio of the PA bead was taken as the ratio of the largest axis length to the smallest axis length.

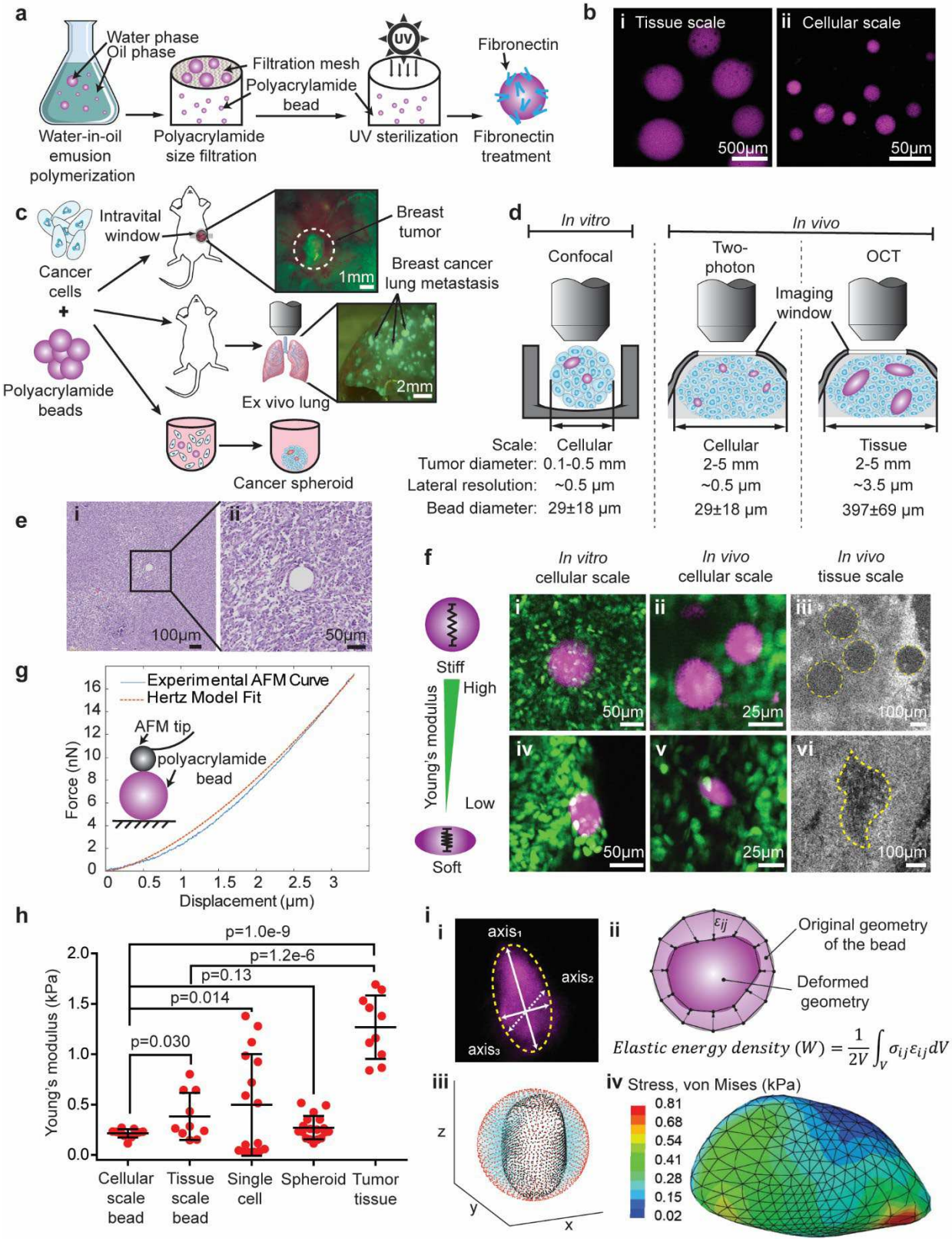

Figure 1|The workflow of *in vivo* solid stress measurement in primary and metastatic tumors. a, Polyacrylamide bead solid stress sensor fabrication, filtration, UV sterilization, and treatment with fibronectin. **b,** Rhodamine-labelled PA beads are

fabricated at the cellular and tissue scales with diameters of 28.7 ± 18.2 μm (mean ± STD, n=8 beads) and 397 ± 69 μm (mean ± STD, n=5 beads), respectively. **c,** To probe solid stresses *in vivo*, breast cancer cells (MCa-M3C HER2/neu+) are injected with PA beads into the mammary fat pad of female FVB/NJ mice and an intravital window is implanted to visualize the PA beads and cancer cells. To probe solid stresses in lung metastases, same cancer cells are injected with PA beads into the tail-vein of female FVB/NJ mice. To probe solid stresses *in vitro*, MCa-M3C-H2B-dendra2 breast cancer cells are seeded with PA beads to form spheroids in low-attachment round-bottom wells. Fluorescent tumors above 1mm in diameter were visualized using a fluorescent stereomicroscope. **d,** Multi-modal intravital microscopy including confocal, two-photon, and optical coherence tomography, were utilized to probe solids stresses *in vitro*, *in vivo* at the cellular scale, and *in vivo* at the tissue scale, respectively. **e,** H&E staining shows the region around the embedded PA beads is similar to regions far from the void, demonstrating no additional fibrosis or inflammation due to PA beads. **f,** The PA bead Young's modulus was optimized at each *in vivo* scale to achieve sensitive measurements of solid stress **(i,ii,iv,v)** cancer cells (green), PA beads (magenta), **(iii,vi)** PA bead (dark gray, yellow dotted outline)). The Young's modulus of the polyacrylamide bead needs to be tuned according to the stress magnitude of interest. Beads with large Young's modulus, E=1.27 ± 0.3 kPa in **(i)**, E=1.27 ± 0.3 kPa in **(ii)**, and E=3.44± 0.3kPa in **(iii)** do not deform in response to solid stresses, and hence will not be sensitive to stresses as shown. The optimal Young's moduli that sensitively deform in response to solid stresses are determined as E=0.21 ± 0.04 kPa for cellular scale *in vitro* **(iv)**, E=0.21 ± 0.04 kPa for cellular scale *in vivo* **(v)**, and E=0.38± 0.15 kPa for tissue scale *in vivo* **(vi)**. **g,** Polyacrylamide bead Young's modulus was measured using AFM and fitting a Hertz model. **h,** AFM measurements of Young's modulus of cellular- and tissue-scale PA beads (mean ± STD, n=10-11 beads, 2-sample t-test), in comparison with Young's modulus of individual cancer cells, spheroids, and tumors formed from the MCa-M3C-H2B-dendra2 cell line (mean ± STD, n=16 single cells, n=18 spheroids (50k cells/spheroid), n=10 tumor regions, 2-sample t-test). **i,** Quantification of solid stress by **(i)** fitting an ellipsoid to obtain 3 axis diameters representing the PA bead and measuring the aspect ratio of PA beads as a simple and accessible readout. The **(ii)** elastic energy density (W) and **(iv)** solid stress spatial distributions are quantified through mathematical modeling by determining the **(iii)** deformation of the bead from the undeformed spherical geometry and finite element analysis.

Validation and sensitivity analysis of the solid stress measurement method *in vivo*

Using intravital microscopy of deformable PA beads, we quantified solid stresses in *in vivo* murine tumors at the cellular and tissue scales in 3-D (Fig. 2a-d). Tumors with cellular-scale beads were formed separately from tumors with tissue-scale beads. We measured the bead aspect ratios after pushing them through 25G and 23G needles (for cellular and tissue scale, respectively) used for tumor injections and our analysis shows that the beads exhibited an aspect ratio of approximately 1 before injecting them into mice (Fig. S7). When PA beads are injected into the mammary fat pad without cancer cells and immediately imaged, the aspect ratios of the beads are 1.26 ± 0.10 (Fig. S7), suggesting that the baseline mechanical stress applied to the spheres by surrounding normal tissue is much smaller than the deformation measured in the presence of tumors. 5-7 days after injecting the PA beads and MCa-M3C-H2B-dendra2 cancer cells into the mammary fat pad of mice, we observed unexpectedly dramatic deformations in the PA beads with an aspect ratio of 3.41 ± 0.59 (mean ± STD, N=4) *in vivo* at the tissue scale measured via OCT (Fig. 2b), and aspect ratio of 1.87 ± 0.42 (mean ± STD, N=3) *in vivo* at the cellular scale measured via two-photon microscopy (Fig. 2d). Thus, we next sought to determine if the deformation was plastic (irreversible) or elastic (reversible), and if the beads were still intact or broken. To investigate this, we used enzymatic dissociation of the tumor as an effective method to relax the intratumoral solid stresses[11,22,26,38,39] to observe the relaxation of the highly deformed PA beads to their original stress-free geometry. For the *in vivo* setting, we used a solution of collagenase and hyaluronidase immediately post-euthanasia *in situ*, and longitudinally imaged the relaxation of the solid stress reflected by a change in the geometry of the PA beads using two-photon microscopy and OCT. For the *in vitro* setting, we used trypsin instead of collagenase and hyaluronidase to dissociate the spheroids since trypsin was sufficient for complete spheroid dissociation. At both the tissue and cellular scales *in vivo* and at the cellular scale *in vitro*, we observed that the beads converge towards the original spherical geometry represented by the aspect ratio of 1 (Fig. 2a-f). This result showed that the PA beads, even being highly

deformed to an aspect ratio of 6, undergo primarily reversible and elastic deformation. In 2-3 hours, the stresses that accumulated in the tissues for 5-7 days could be relaxed using enzymatic dissociation of tissue. While the beads relaxed to an aspect ratio of close to 1 in the *in vitro* spheroids where enzymatic dissociation was more effective, the *in vivo* beads did not fully relax to an exact aspect ratio of 1 potentially due to residual stresses that may have remained due to incomplete dissociation of surrounding tissue (Fig. S7). We did not fully dissociate the tissue mechanically in order to maintain the relative position of beads during longitudinal tracking of the beads over the course of enzyme dissociation. In the time and length scales of this study, the viscoelastic effects are negligible since the relaxation time of polyacrylamide is much shorter (< 4 minutes; Fig. S8) than the 2-3 hours of stress relaxation by enzymatic dissociation. Thus, the PA beads underwent a dramatic but reversible deformation demonstrating that this method can be used to sensitively measure a wide range of solid stress magnitudes.

We next investigated if euthanasia affected the measurement of solid stress, and whether the solid stresses and interstitial fluid pressure (IFP; another physical hallmark of cancer that is elevated in tumors[1]) were coupled. There has been recent controversy about the coupling of IFP and solid stresses and the consequences of this coupling in fibrotic tumors; hence, it is critically important to probe the distinction between solid stress and IFP due to their distinct consequences[22,40,41]. To decouple fluid pressure from solid stresses, we euthanized mice to relax the IFP, which originates from blood pressure and converges to zero post-mortem[40,42], and compared the deformation of the PA beads *in vivo* versus 60 minutes post-mortem. Interestingly, we noticed that at both the cellular and tissue-scales, euthanasia, and hence relaxation of IFP, did not significantly affect solid stress levels: solid stress measured up to 60 minutes after euthanasia closely reflected the *in vivo* solid stress values (Fig. 2g).

Finally, we optimized and validated our tumor induction approach to exclude any potential artifact, e.g., artificial compression exerted by the window. We compared the solid stress at the cellular level in tumors that were induced after the implantation of the imaging window versus tumors growth without any imaging window to avoid potential artificial compression. We did not observe any significant difference between the solid stress in these two tumor induction methods (Fig. 2h), and concluded that tumor induction under the imaging window did not alter the intratumoral solid stresses. As a negative control, we observed that if the imaging window was implanted over established tumors, the window may artificially compress the tumor and generate an artifact in the solid stress field (Fig. S9). Hence, for studies relevant to the physical tumor microenvironment, implantation of windows over established and large tumors should be avoided.

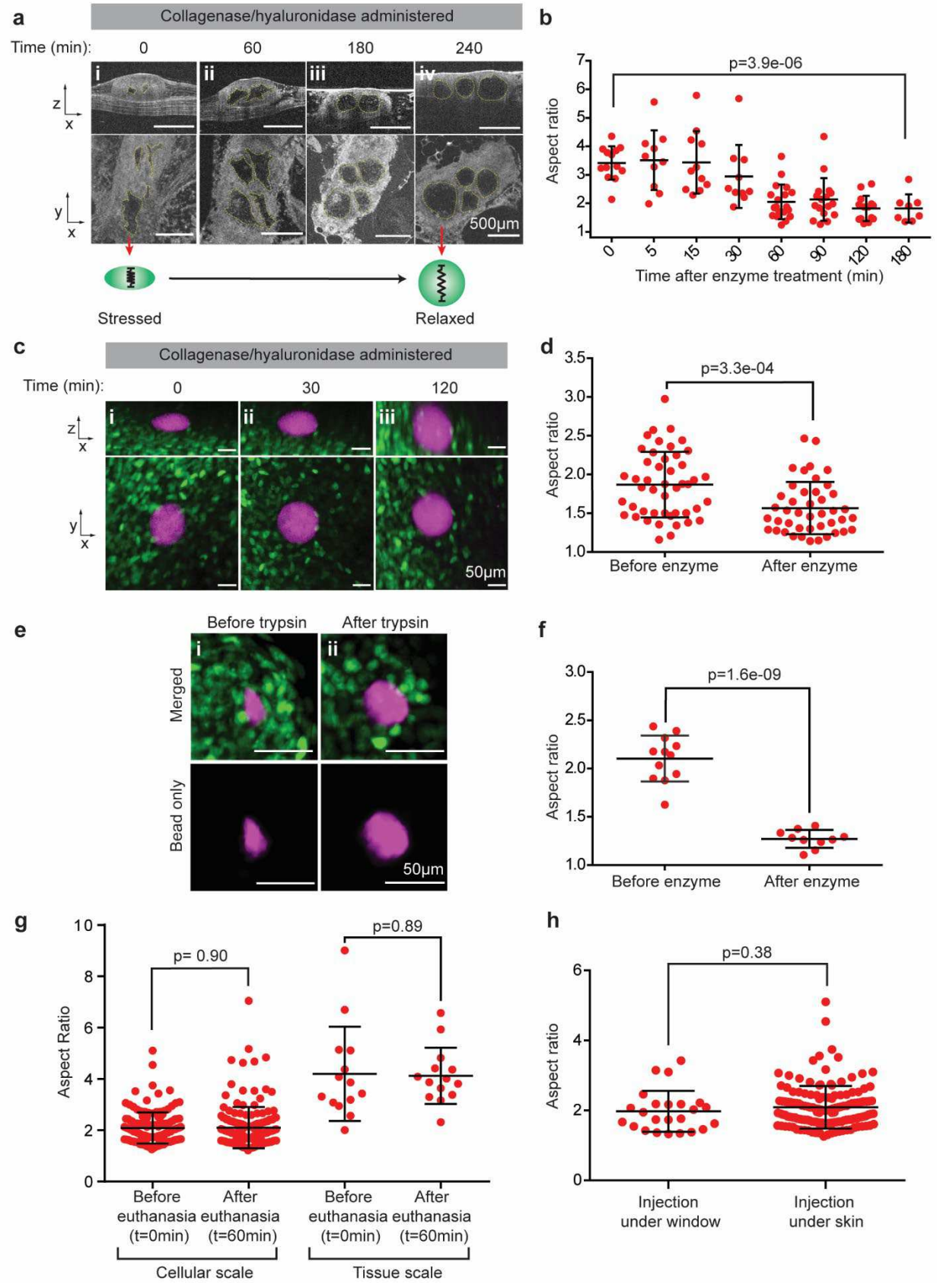
a
Collagenase/hyaluronidase administered
Time (min):
0
60
180
240
i
ii
iii
iv
z
x
y
x
500μm
Stressed
Relaxed
b
p=3.9e-06
Aspect ratio
Time after enzyme treatment (min)
c
Collagenase/hyaluronidase administered
Time (min):
0
30
120
i
ii
iii
50μm
d
p=3.3e-04
Aspect ratio
Before enzyme
After enzyme
e
Before trypsin
After trypsin
Merged
Bead only
50μm
f
p=1.6e-09
Aspect ratio
Before enzyme
After enzyme
g
p= 0.90
p=0.89
Aspect Ratio
Before euthanasia (t=0min)
After euthanasia (t=60min)
Before euthanasia (t=0min)
After euthanasia (t=60min)
Cellular scale
Tissue scale
h
p=0.38
Aspect ratio
Injection under window
Injection under skin

Figure 2| Validation and sensitivity analysis of solid stress measurement at the cellular and tissue scales *in vivo.* **a,** Relaxation of solid stresses at the tissue scale was demonstrated by enzymatic treatment (collagenase/hyaluronidase) of the tumor *in situ* post-euthanasia and imaging of the beads with optical coherence tomography (OCT) (PA beads marked with yellow dotted line). Tracking highly deformed beads relaxing to near-spherical geometry demonstrates the presence of extremely high stresses that were able to deform the PA beads to otherwise unrecognizable geometries. The reversibility of PA bead deformation (**i** to **iv**) demonstrates their sensitivity and wide dynamic range of solid stresses that can be quantified from their experienced deformation. **b,** Dynamics of aspect ratio after collagenase/hyaluronidase treatment at the tissue scale *in situ*. (mean ± STD, N=2-4 mice, n=8-19 beads, 2-sample t-test)**. c,** Representative multi-photon images from administration of collagenase/hyaluronidase enzyme at the cellular scale *in situ* (cancer cells (green), PA beads (magenta)). **d,** Aspect ratio of the cell-scale beads converges to 1 (spherical geometry) after collagenase/hyaluronidase treatment. (mean ± STD, N=3 mice, n=4 beads, 2-sample t-test). **e,** Representative confocal images of a spheroid embedded with a polyacrylamide bead before and after trypsin treatment (cancer cells (green), PA beads (magenta)). **f,** Stress relaxation after trypsin treatment. (mean ± STD, n=13-36 beads, 2-sample t-test). **g,** Euthanasia and the consequent changes in IFP does not significantly change the solid stress levels at the cellular and tissue scale (mean ± STD, N=4 mice, n=14-21 beads, 2-sample t-test). **h,** After injecting tumor cells under an already implanted window, we found that the presence of the imaging window chamber does not alter the solid stresses measured at the cellular scale (mean ± STD, N=4-7 mice, n=33-151 beads, 2-sample t-test).

Scale-dependent transmission of solid stresses

Tumors have heterogeneous mechanical properties and architecture across different length scales[43,44]. We used our *in vivo* solid stress measurement method to investigate if solid stresses are length-scale dependent in tumors. To measure solid stresses at the cellular and tissue scales, the PA bead sizes were fabricated to mimic cellular- and tissue-length scales (28.7 ± 18.2 μm and 397 ± 69 μm in diameter, respectively (Fig. 3a)). Surprisingly, the elastic energy density and maximum principal solid stress at the tissue scale was measured to be significantly higher (5x and 6x, respectively) than that of the cellular scale (Fig. 3b,c). This was unexpected, as the stress (force normalized by area), and strain energy density (elastic energy normalized by volume) do not depend on the scale of measurement in homogeneous and linear materials. Furthermore, when compared to solid stress values quantified via previous *ex vivo* methods[26,27], the *ex vivo* quantification of solid stress is in the range of cellular-scale stresses, but vastly underestimates tissue-scale stresses (Fig. 3c), demonstrating that in the previous ex vivo methods, the solid stress was only partially relaxed and measured. Using a simplified quantification of solid stress via the measurement of aspect ratios, we also observed that tissue scale PA beads were deformed at a significantly higher (2x) aspect ratio than the cell scale beads (Fig. 3d). The factor of difference in aspect ratios measured at the cellular vs tissue scale (2x) is lower than the factor of difference in maximum principal solid stress (6x). The difference in Young's moduli between the cellular-scale and tissue-scale beads likely contributes to this discrepancy since the tissue-scale PA beads have a higher Young's modulus compared to cellular-scale PA beads (Young's modulus of 0.215 ± 0.042 kPa at the cellular scale and 0.383 ± 0.234 kPa at the tissue scale). It would be expected that if cellular- and tissue-scale beads have the same Young's moduli, the factor of difference in the aspect ratios between the cellular and tissue scales would be more reflective of the factor of difference in maximum principal solid stresses. Additionally, when we collectively injected cellular-scale beads of 28.7 ± 18.2 μm in the same tumor, we consistently noticed an increasing trend in aspect ratio as the PA bead diameter increased (Fig. 3e), further demonstrating the scale-dependence of solid stress in tumors. In the bulk of our analysis, the elastic energy density and solid stress values were obtained by approximating the PA beads to ellipsoids, but by using the original deformed geometry of the bead in our FEM model, we demonstrated that at the cellular-scale beads experienced a narrow range of stresses, whereas tissue-scale beads experienced a wider range and larger magnitude of stresses (Fig. 3f). By using the original deformed geometry of the bead, we were able to capture differences in spatial heterogeneity experienced at the cellular and tissue scales; we showed that the tissue-scale

measurements capture heterogeneity in solid stresses, whereas the solid stresses experienced at the cellular scale are comparatively more uniform.

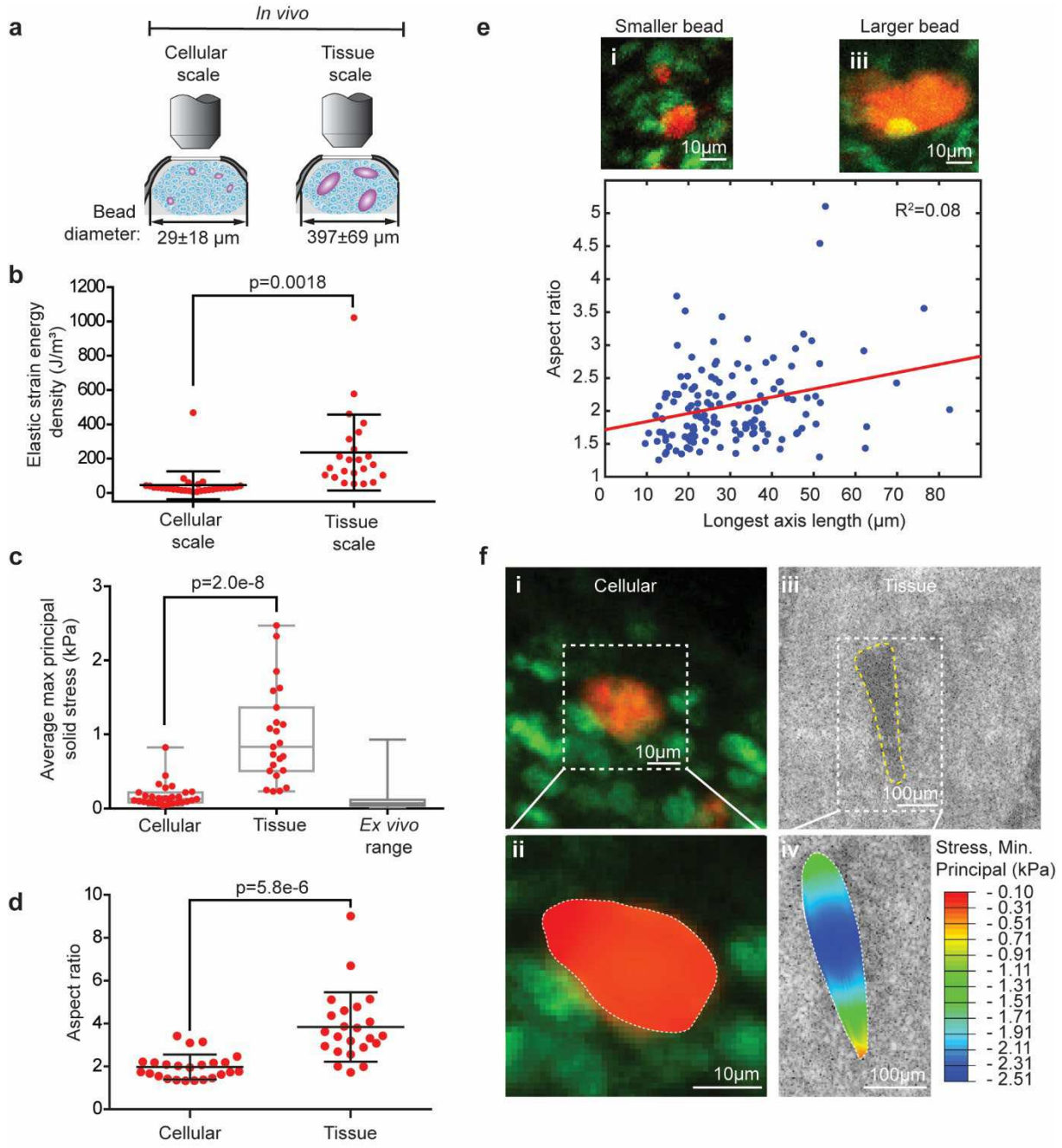

Figure 3|Solid stress transmission is scale-dependent: *In vivo* solid stresses experienced by cancer cells at the cellular scale is significantly lower than solid stresses experienced at the tissue scale. a, Measuring solid stresses across an order of magnitude different scales. **b,** Elastic energy density of *in vivo* tumors at the tissue scale (236 ± 220 J/m^3) is higher than the cellular-scale energy density (45.1 ± 81.9 J/m^3) by approximately a factor of 5 (mean ± STD, N=5 mice, n=23-30 beads, 2-sample t-test). **c,** Average maximum principal solid stress of *in vivo* tumors is 6x higher at the tissue scale (0.978 ± 0.64 kPa) compared to the cellular scale (0.172 ± 0.15 kPa) (mean ± STD, N=5 mice, n=23-30 beads, 2-sample t-test). Comparison with the solid stress range (σ_{zz}) in an *ex vivo* tumor measured using previous methods[26,27] demonstrates that previous methods do not represent the full range of 3-D solid stresses in an *in vivo* tumor. **d,** Aspect ratios of the polyacrylamide bead *in vivo* at the cellular scale is 2x higher

compared to the tissue scale. (mean ± STD, N=5 mice, n=23-30 beads, 2-sample t-test). **e,** Scale-dependence of polyacrylamide bead deformation within cellular-scale sized beads imaged in the same tumor by two-photon microscopy (cancer cells (green), PA beads (red)). Positive relationship of aspect ratio with increasing polyacrylamide bead diameter (n=143 beads, linear regression, R^2= 0.08, p-value = $6.6x10^{-4}$). When cellular-scale polyacrylamide beads, which varied from 28.7 ± 18.2 µm in diameter, were used, the increasing trend in scale-dependence with solid stress is consistent with the results reported in (**b-d**). **f,** Finite-element modeling of polyacrylamide beads enables quantification of the spatial distribution of solid stresses at the cellular and tissue scales (**(i)** cancer cells (green), PA beads (red), **(ii)** Overlay of cellular-scale FEM stress-distribution cross-section, **(iii)** PA bead (yellow dotted outline)). **(iv)** Overlay of tissue scale FEM stress-distribution cross-section.

In vitro 3-D cancer model recapitulates *in vivo* tumor solid stress at the cellular scale

Spheroid and organoid models of tumors are increasingly popular because they better recapitulate the 3-D architecture and cellular organization of tumors. However, it is not known whether they faithfully recapitulate the abnormal biophysical tumor microenvironment of *in vivo* tumors. To answer this question, we used our solid stress measurement method to compare solid stresses in spheroids and *in vivo* tumors (Fig. 4a). Since spheroids cannot be too large (diameter >500 µm) due to formation of necrosis[45], we only compared solid stresses measured at the cellular scale, and not at the tissue scale. Unexpectedly, we observed that the solid stresses in spheroids were not significantly different from those measured *in vivo* (Fig. 4b). Furthermore, we observed that cellular-scale solid stresses did not depend on the size of the spheroids, as determined by seeding density of the cancer cells (Fig. 4b). The similarities of solid stresses in spheroids, which were formed by cellular aggregation in 24-48 hours, and *in vivo* models, which were formed in a few days with stromal recruitment, implied that the cell-cell interactions played a major role in the genesis of solid stresses, and that the magnitude of solid stress was independent of the number of cells in the multi-cellular aggregates.

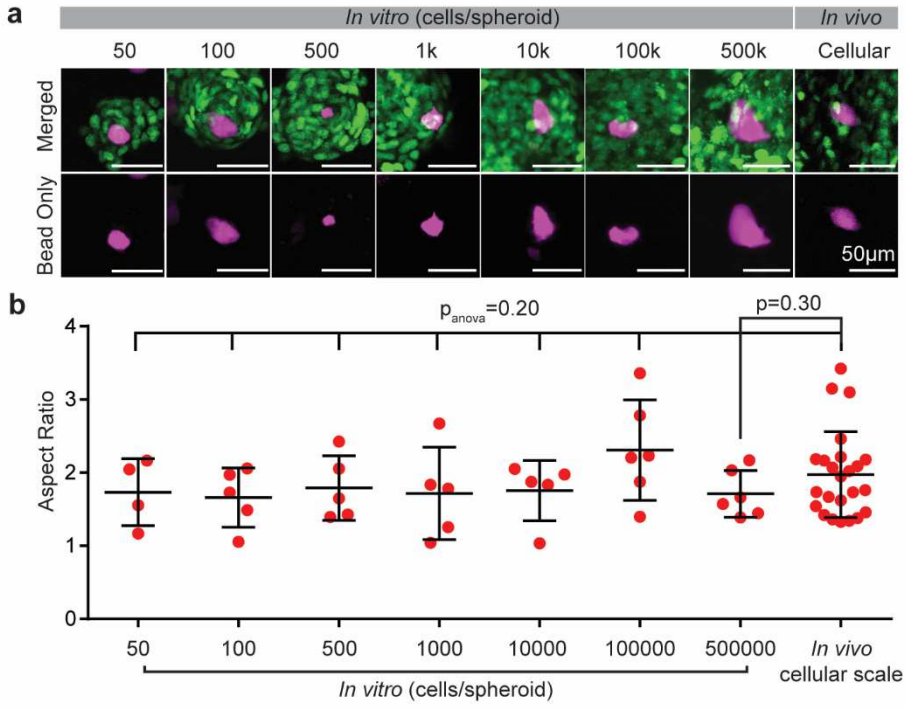

Figure 4| *in vitro* models of tumors faithfully model the solid stresses levels *in vivo* at the cellular scale. a, Representative images of spheroids at multiple seeding densities (2 days after seeding) and *in vivo* cellular scale (5 days after injection) (cancer cells (green), PA beads (magenta)). **b,** Aspect ratios of *in vitro* spheroids do not vary significantly by seeding density (mean ± STD, N=5-6 spheroids, one-way ANOVA, Tukey's multiple comparisons test) demonstrating the independence of solids stresses

and the spheroid size. Aspect ratios of PA beads embedded in spheroids compared to *in vivo* cellular scale PA beads are not significantly different (mean ± STD, N=5 mice, n=24 beads, 2-sample t-test) demonstrating that spheroid models recapitulate *in vivo* cellular-scale solid stresses.

Measurement of solid stresses in lung metastasis

Given that there is evidence that metastatic and primary tumors, despite originating from the same cancer cells, have distinct reponse to treatment[46], we decided to quatify solid stress in the breast cancer lung metastasis. While the physical microenvironment of metastatic tumors have been characterized in liver[26] and brain[20], the mechanical environment of lung metastasis is poorly understood due to the complex structure of the lung. To measure solid stress in metastatic lung tumors, we co-injected PA beads with the same breast cancer cells (MCa-M3C-H2B-dendra2) into the tail-vein of mice. The goal was to have the fluorescent PA beads and cancer cells travel through circulation to the lung and form a metastatic tumor, and by measuring the deformation of the bead, we then estimated the solid stresses in the breast cancer lung metastasic tumors. After approximately 4 weeks, we sacrificed the mice and extracted the whole lung for *ex vivo* imaging of the pleural lung surface. Interestingly, the beads sequestered in the lung vasculature in regions with and without metastatic cancer nodules. The beads, with average diameters of 40μm, are arrested at the arteriole-capillary junction as they are too large to travel through pulmonary capillaries (Fig. 5a). Since the beads are at the same scale and have a similar Young's modulus as cancer cells (Fig. 1h), the bead deformation reflects the stresses that single cancer cells experience inside small vessels in the lung. The magnitude of solid stress that the beads experience was estimated via finite element modeling to be as high as 0.73 kPa (Fig. 5a(ii,iv)), which resulted in substantial deformation in the PA beads. To our knowledge, this is the first direct estimation of the stresses that a circulating cell experiences inside the pulmonary microvasculature. While we have measured the stresses that individual cells experience at a static setting in a lung, these stresses are cyclic in a respiring lung; therefore, cells traveling through vessels in a respiring lung would experience different magnitudes of cyclical stresses that activate biological processes requiring cyclical mechanical forces[47–49]. This method to estimate the stresses applied on the circulating cells in the lung capillaries is not limited to cancer cells, and can be extended to estimate the solid stresses that immune cells experience during their sequestration in the lung capillaries and how these mechanical forces affect their function[47].

We also observed deformed PA beads in breast cancer lung micrometastiasis with a scattered distribution of cancer cells (Fig. 5b(ii)). We observed no significant differences in bead aspect ratio between the non-metastatic and micrometastatic regions (Fig. 5c). This observation implies that the stresses imposed on beads by the lung vasculature dominate over the stresses generated by the micrometastasis. We anticipated that in the case of macrometastasis, with established and dense tumors as opposed to the sparse clusters cancer cells that occur in micrometastasis, the solid stress levels will be much higher than in micrometastasis, as observed previously in the context of lymph node metastasis[26], and would result in additional deformation of the PA beads. We also compared bead aspect ratios between primary vs lung micrometastatic cancer (Fig. S10), but observed no significant difference, which could imply that micrometastases in the lung experience similar levels of solid stress as the primary tumor cells. However, since the lung metastasis model was imaged *ex vivo*, we expect cancer cells in lung micrometastases to experience higher stresses during lung inspiration. Additionally, we investigated whether PA beads arrested in the lung vasculature are sensitive to lung inflation. We imaged the PA beads before and after inflation with phosphate buffered saline (PBS) and noticed further deformation in the PA bead (Fig. 5d). The aspect ratio of the deflated and inflated PA beads were 2.10 and 2.67, respectively.

The maximum absolute values of the principal stress component of the PA beads for the deflated and inflated state were 0.6 kPa and 0.68 kPa, respectively. Therefore, the PA beads are sensitive to changes in solid stress even when deformed. This can be used to detect cyclical changes in vasculature during respiration to determine the changes in solid stress experienced by cells in vessels.

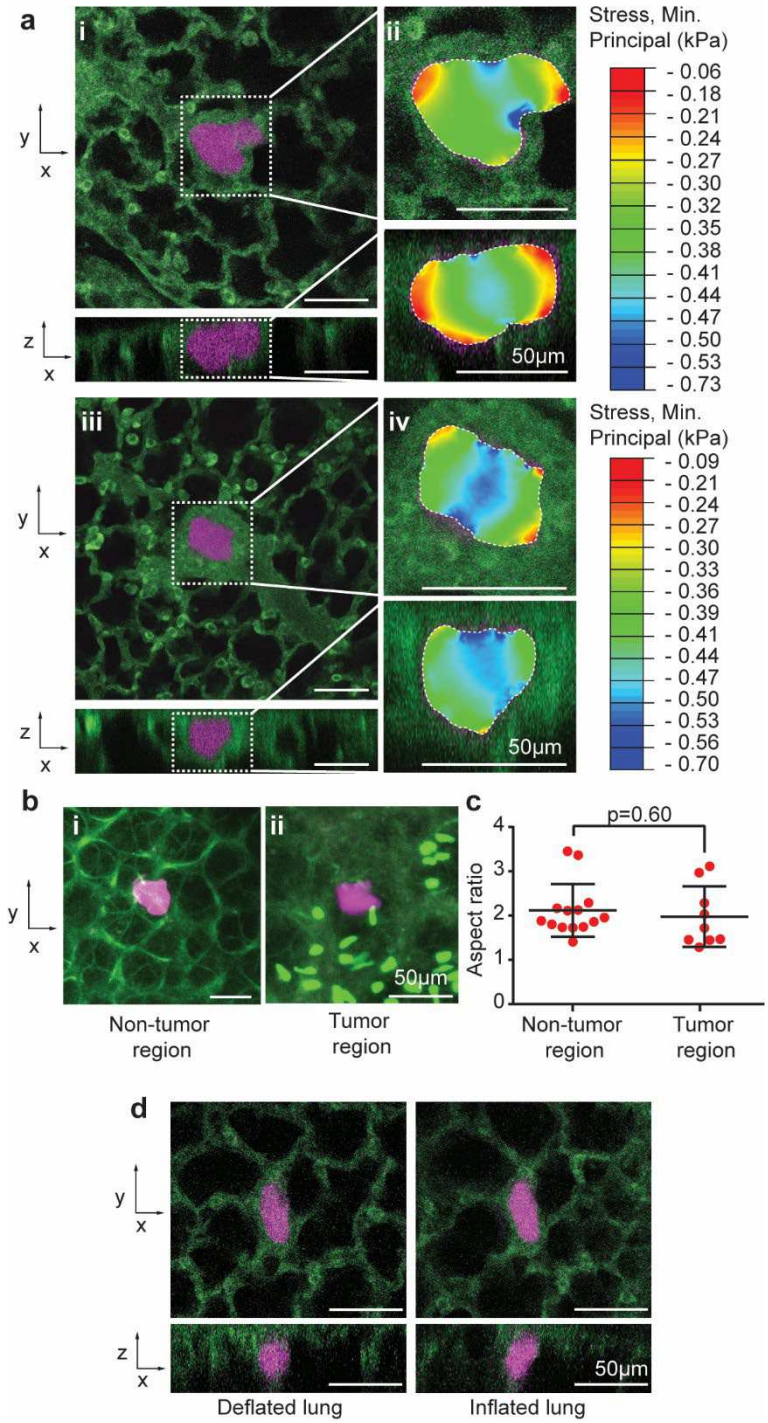

Figure 5|Direct measurement of solid stresses that individual cells experience in lung metastasis. a, (i,iii) Representative images of cellular-scale bead in regions of the lung without cancer metastasis. The PA beads with similar size and stiffness as the individual cancer cells traveled to the lung through the blood circulation and arrested in microvasculature (lung autofluorescence from

extracellular matrix proteins (green), PA beads (magenta)). **(ii, iv)** Finite-element modeling to visualize stress mapping of the polyacrylamide bead at high-resolution in the lung that demonstrates the cancer cells experience stresses as high as 0.73 kPa during their microvascular arrest in lung metastasis (lung autofluorescence (green), PA beads (magenta)). **b,** Representative image of PA beads arrested in non-tumor and tumor regions of the lung (lung autofluorescence (green), cancer cell nuclei (green), PA beads (magenta)). **c,** Comparison of aspect ratio of polyacrylamide beads in the normal vs micrometastasis in the lung demonstrates that the stresses exerted by the arterioles are the dominant cause of deformation in the beads. (mean ± STD, N=2-3 mice, n=9-14 beads, 2-sample t-test). **d,** PA beads in the lung vasculature deforms when the lung is inflated (lung autofluorescence (green), PA beads (magenta)), demonstrating the capability to measure the cyclic solid stresses that individual cells experience during the breathing cycle.

Discussion

We report the first *in vivo* measurement of solid stresses in mouse models of primary breast cancer and breast cancer lung metastasis. There are four (i-iv) key advantages of our method over existing methods. (i) Longitudinal monitoring of the solid stress, as opposed to the terminal point measurements in existing methods, is critical to characterize the role of solid stress in tumor progression and treatment response. We demonstrate this capability by longitudinally monitoring the stress relaxation *in vivo*. Additionally, we show that interstitial fluid pressure, which is elevated only in the *in vivo* tumors, is not coupled to solid stresses using a post-euthanasia model. (ii) Our *in vivo* method allows multi-scale measurement of the solid stresses. Previous methods report solid stresses in sub-millimeter resolution[26,27] while our *in vivo* methods, which relies on optical resolution, estimates solid stresses more precisely at higher resolutions at the tissue and cellular scale, where tumors cells directly sense and respond to solid stress. This cellular-level capability enables the measurement of solid stress that individual cells experience in lung capillaries, a determination unachievable with existing low resolution methods[26,27]. (iii) Our method affords a measurement of the full magnitude and direction of solid stresses. Previously developed *ex vivo* methods rely on a mechanical relaxation of the stress in the form of cutting or slicing the tumor[26,27], which relaxes solid stresses only partially in certain directions. With our method, the full solid stress at a given point is reported as a tensor, which provides both magnitude as well as direction of the stress components. (iv) Finally, our method accounts for solid stress exerted by surrounding normal tissues since tumors are retained *in situ* and are not excised. In the previously reported *in situ* solid stress measurement method, accounting the solid stress exerted by surrounding tissues can cause solid stress measurements in the tumor to be a factor of 5 higher than the intratumoral stresses measured after the tumor has been excised[26].

With our *in vivo* characterization of solid stresses in breast tumors, we observed the surprising phenomenon that solid stress transmission is scale dependent. In a homogenous material, it is expected stresses at the cellular scale to be similar in magnitude to stresses at the tissue scale, as stress is normalized by length scale. On the contrary, we observed that tumor cells experience 6x lower solid stresses at the cellular scale compared to the tissue scale. Given the immense biological and immunological implications of this finding with regards to the transmission of intratumoral solid stresses to tumors and immune cells, we tested for biases in our experimental parameters through multiple approaches. First, in addition to stresses, we report elastic energy density and aspect ratio of the deformed beads, which are both normalized to the scale of the bead. In both readouts, we observe consistently larger solid stresses at the tissue scale compared to cell scale. Second, since the cellular level and tissue level measurements are performed in different experiments and mice, potential biases due to multi-cohort experiments are eliminated by measuring the solid stresses in a heterogeneous population of bead sizes (28.7 ± 18.2 μm) in the same mouse. Solid stresses deform large beads at a higher magnitude

compared to smaller beads, consistent to the scale-dependence we observed in the much larger PA beads. The discerned scale-dependence in small vs large cell-sized beads in the same region of interest and using the same imaging modality (two-photon) further confirms our observation of increasing solid stress transmission with increasing PA bead size that we observed in cell- vs tissue-scale beads.

One of the key implications of the scale-dependence of solid stresses is the potential biophysical mechanism(s) that tumor cells utilize to protect themselves against the lethally high solid stresses that exist at the tissue level. We show that growth-induced solid stresses generated at the tissue level can be as high as about 2.5kPa (Fig. 3c), which is consistent with the previous *ex vivo* measurements[26]. Such high mechanical stresses can be lethal to cells[32,33,34] given that the Young's modulus of individual cells is about 1kPa (Fig. 1h) and such high stresses would result in deformation of up to 50% of the cell diameter (Fig. 3c). Since the first measurement of solid stresses[13,26], the question of how tumor cells tolerate such high solid stress values has remained unanswered. Furthermore, recent studies show that solid stresses of ~0.1kPa damage and kill the cells in the normal tissue surrounding the tumor[20,21], which further amplified the dilemma on the differential response of tumor vs normal cell to solid stresses: if the compressive forces that tumors apply on normal tissue are equally felt by the tumor cells, why are cells in the normal tissue succumbing to solid stresses while tumor cells are proliferating? A recently proposed biological mechanism to protect tumor cells against high levels of solid stress is the loss of p53 which enables neoplastic cells to be more resistant to high mechanical stress levels[5,34]. However, p53 is not universally mutated in all tumor cells, and such mechanical resistance phenotypes only apply to cancer cells with certain mutations and not to the intratumoral stromal cells without any mutation in p53. Therefore, we propose that the existence of biophysical mechanisms that dissipates the high macroscale solid stresses to much lower levels at the cellular scale could better explain how cancer cells, tumor-associated immune cells, fibroblasts, and blood vessels can tolerate solid stresses.

Another key implication of the solid stress scale-dependence is the differential compression of small vs large blood vessels in the tumors. Specifically, solid stresses compress the intratumoral [14,15,23,40,50] and extratumoral blood vessels,[20] which fuels tumor progression and treatment resistance [51]. The scale-dependence of solid stress shows that large vessels, which could be mainly co-opted vessels, likely experience higher magnitudes of solid stress compared to capillaries and smaller vessels, which are more prone to collapse by compression due to lack of pericyte coverage[52]. This transmission of solid stresses within the tumor environment, in a scale-dependent manner, may explain how weak tumor capillaries still function despite the presence of high compressive solid stresses. As a result, this differential stress transmission to blood vessels bears important implications in vascular normalization and decompressing blood vessels by targeting solid stress[23,40,53–55].

While studying the origins of multi-scale transmission of solid stresses is beyond the scope of this study, we propose a hypothesis for the observed phenomena. To withstand high stresses within tumors, cancer and stromal cells may organize the ECM and cellular microarchitecture to generate stiffness heterogeneities at a certain characteristic length scale that dissipate the stresses at the cellular scale through a caging effect. In this proposed mechanism, the surrounding stiffer areas, acting collectively as a cage, protect the cells from excessive deformation. The proposed mechanism is supported by our findings that, in addition to solid stress transmission being larger at the tissue scale, the tissue scale reveals more heterogeneity in stress transmission that is not captured at the cellular scale, as shown by the larger range in stress magnitudes when FEM is performed on the original geometries of the deformed PA beads. This suggests that solid stress in the tumor is highly heterogeneous, yet cells do not experience the same

level of heterogeneity. This supports our proposed mechanism that the caging effect reduces the magnitude of solid stress as well as the level of stress heterogeneity at the cellular scale. Due to the cell-size characteristic length scale of the stiffness heterogeneities, solid stresses compress and deform the tissue at the tissue level while cells experience smaller levels of solid stress. This caging effect may occur in tandem with tissues undergoing macroscale re-alignment to redistribute high mechanical stresses and thereby dissipate mechanical energy as proposed recently as a mechanism of nucleus protection[56]. Such adaptive caging effect is likely specific to the abnormal physical microenvironment in tumors that does not exist in normal tissue, which may explain why the normal tissue surrounding the tumors is more prone to damage compared to the tumor cells, despite experiencing similar levels of solid stresses at their interface[20]. Future studies in which the stiffness heterogeneities of the tumor can be characterized in 3-D and at the cellular resolution may provide more information to decipher the origin of this unexpected observation on the multiscale nature of the mechanical tumor microenvironment. Discovering the mechanism underlying the scale-dependence of solid stress transmission will also inform therapeutic strategies that disrupt the protective tumor microenvironment against solid stresses to increase the sensitivity of cancer cells to high stresses.

We show that our *in vivo* measurement method is also applicable to characterizing the solid stresses that cancer cells experience during metastasis, which can provide insight to the role of mechanical stress on the multistep metastatic cascade. The compression of individual cancer cells migrating through blood and lymphatic vessels affects their extravasation through the vasculature and their subsequent formation of micro- and macrometastasis[1,57]. Our *in vivo* cellular-scale measurement of solid stresses is not limited to cancer cells; it is amenable for studying the mechanosensitivity of immune cells, and provides an estimate of the solid stresses that immune cells experience as they circulate, sequester, and infiltrate into the lung microvasculature[58,59].

In summary, we report the first *in vivo* measurement of intratumoral solid stresses in both the primary and metastatic setting where the complexities of the tumor microenvironment are preserved. Our *in vivo* methods equip cancer researchers with a multi-scale tool to better understand the spatiotemporal co-evolution of the physics, biology, and immunology of cancer. The discoveries that solid stress transmission is scale-dependent and that individual cancer cells experience substantially lower solid stresses than experienced at the macroscale provide important insights for mechano-adaption in tumors. These findings will pave the way for discovering new biophysical mechanisms that cancer and stromal cells utilize to protect themselves against lethally high solid stresses and for novel treatments that alter the solid stresses in the tumor or increase tumor cell sensitivity to solid stresses.

Methods

Polyacrylamide formulation, fabrication, and functionalization

The fabrication of PA beads was performed using water-in-oil stirred emulsion polymerization as described by Lee et al.[28] Polyacrylamide (PA) formulations were prepared to achieve the following Young's modulus (E) by altering the percentages of acrylamide (40% stock, Bio-rad, 1610140) and bisacrylamide (2% stock, Bio-rad, 1610142): E=0.215 ± 0.042 kPa (3% acrylamide, 0.06% bisacrylamide), E=0.38± 0.15 kPa (5% acrylamide, 0.03% bisacrylamide)[60]. PA pre-polymer solutions were prepared in rubber-sealed glass vials and purged with nitrogen gas (N_2) for 15 minutes. The oil phase, kerosene (Sigma-Aldrich, 329460) with 6% w/v PGPR 4150 surfactant (Palsgaard, 90415001) was prepared in an Erlenmeyer flask and purged with N2 for 30 min. To 1 mL of pre-polymer mixture, 10 µL of 10% w/v methacryloxyethyl

thiocarbamoyl rhodamine B (Polysciences, 23591-100) in dimethyl sulfoxide (DMSO) was added, followed by 100 µL of 1% w/v ammonium persulfate (APS; Bio-rad, 1610700) in phosphate buffered saline (PBS) and 5 µL of tetramethylethylenediamine (TEMED; Sigma-Aldrich, T7024).

The pre-polymer solution was injected into the oil phase and the emulsion was vortexed for 10s. The emulsion was magnetically stirred at 300-600 rpm (300rpm for tissue-scale beads and 600rpm for cellular-scale beads) for 60 minutes while the beads polymerized. The beads were centrifuged to remove the kerosene with surfactant and subsequently cleaned with kerosene to remove remaining surfactant. The beads were recovered in PBS through multiple centrifugation steps.

Beads were filtered to tissue-scale (397 ± 69 µm in diameter) or cellular-scale (28.7 ± 18.2 µm) sizes using stainless steel wire cloth (McMaster) fitted to custom-designed filter holders. The beads were then sterilized under UV light for 15 minutes and swelled overnight in PBS at 4°C. Beads were resuspended in 0.05 mg/mL Sulfo-SANPAH (G-Biosciences, BC38) in PBS and irradiated under UV light for 4 min to activate the cross-linker. Beads were rinsed with PBS, and resuspended and incubated overnight in 40 ug/mL fibronectin (Sigma Aldrich, F1141) to allow for cell adhesion and promote uptake of beads by the tumor. The fibronectin-treated beads were resuspended in PBS and stored at 4°C in low adhesion microcentrifuge tubes to prevent beads from adhering to the tube. Fibronectin-treated beads are fluorescent and cell-adherent for at least 1 year after fabrication when stored in isotonic PBS at 4°C.

Cell culture

The MCa-M3C HER2/neu+ with H2B-labelled dendra2 (*Her2*+, *p53*+) cell line (MCa-M3C-H2B-dendra2) is a highly metastatic HER2/neu+ mammary tumor line derived from the MMTV-PyVT/FVB transgenic mouse[36,50,61]. MCa-M3C-H2B-dendra2 cells were cultured in Dulbecco's Modified Eagle's medium with L-Glutamine, 4.5g/L Glucose and Sodium Pyruvate (DMEM; Corning) supplemented with 10% fetal bovine serum (FBS; Fisher Scientific, SH3039603) and 1% antibiotic-antimycotic (Fisher Scientific, 15240062) at 37 °C and 5% CO_2. Cells were harvested at ~80% confluency, counted and resuspended in DMEM. All cell lines repeatedly tested negative for mycoplasma using the Mycoalert Plus Mycoplasma Detection Kit (Lonza, Allendale, NJ).

Culture of beads in spheroids for *in vitro* measurements of solid stress

Spheroids were cultured in 96-well Clear Round Bottom Ultra-Low Attachment Microplates (Corning, 7007) with 500 to 500,000 cells per well to form spheroids of different sizes. Between 1-10 fibronectin-functionalized beads were seeded per well in accordance to the number of cells seeded per spheroid. More beads were seeded for larger spheroids in order to increase the probability that a bead would end up at a depth in the spheroid that could be imaged via confocal microscopy. The plate was centrifuged at 1200 rpm for 10 minutes to coalesce the cells and beads. The spheroids were cultured at 37 °C and 5% CO_2 for 24 to 48 hours. As cells coalesce to form spheroids, beads become embedded within the spheroid and may end up anywhere from the core to the edge of the spheroid.

Tumor Models

All animal procedures were approved by the Institutional Animal Care and Use Committee of Boston University.

Primary breast tumor model for in vivo measurements of solid stress

Tumors were formed either via injection into the mammary fat pad under intact skin or injection under the intravital window into the mammary fat pad. Approximately 10 (tissue-scale: 397 ± 69 μm in diameter) or 50 (cellular-scale: 28.7 ± 18.2 μm) fibronectin-functionalized beads and $1x10^6$ MCa-M3C-H2B-dendra2 cells[36] (*Her2*+) in 50 μL of DMEM were co-injected into the mammary fat pad of 6-8 week old female FVB/NJ mice (JAX). Tumors were grown for 5-7 days and resulted in a palpable mass when cancer cells were injected under the skin (Fig. S11). For tumors grown via injection under the window, a stereomicroscope with a GFP filter and blue light excitation was used to confirm presence of fluorescent mass under the window. Tumors were size-matched for cellular and tissue scale experiments (tumor dimensions: ~3x3mm to 6x6 mm).

Lung metastasis model for ex vivo measurements of solid stress

Approximately 50 cellular-scale fibronectin-functionalized microbeads and $1x10^6$ MCa-M3C-H2B-dendra2 cells were co-injected via tail-vein into 6-8 week old female FVB/NJ mice (JAX). Lung metastases between ~100 μm to 2mm formed ~4 weeks after injection; large metastatic nodules were identified via blue light excitation and GFP filter using a stereomicroscope. The same lung with metastases had non-tumor and tumor regions. Non-tumor regions defined as regions of the lung without any cancer cells present within a 500μm radius.

Tumor induction under intravital mammary window

Multiple methods of tumor induction under the window were investigated. Injecting cancer cells and PA beads directly under the window with and without Matrigel did not result in formation of tumors. Stereotactic injection of the cancer cells and PA beads under a thin layer of tissue under the window resulted in formation of tumors, as confirmed using a fluorescent stereomicroscope. While injection of Matrigel directly under the window did not form tumors, it did allow for enough contrast for visualization of tissue-scale beads at day 0 of injection (Fig. S12). For future experiments, injection of Matrigel with cancer cells and beads can be performed stereotactically under a thin layer of tissue for tracking of tumor formation from day 0 at the tissue scale.

Implantation of window

The Royal Blue SFA Stereo Microscope Fluorescence Adapter (NIGHTSEA) was used to visualize fluorescence under the skin to determine the presence of a tumor. The skin was removed from the tumor and custom-designed, 3D-printed intravital imaging windows (Clear Resin, Formlabs; Fig. S1) were sutured over the mammary fat pad. A 10 mm round coverslip (#1.5 0.16-0.19mm, Ted Pella) was placed onto the window and secured using a metal retaining ring (91580A132, McMaster). For tumors formed after intravital window implantation, $1x10^6$ MCa-M3C-H2B-dendra2 cells were injected as a bolus under a thin layer of tissue under the window. A custom-fitted stainless-steel cover was fabricated to protect the window from mouse chewing.

Lung extraction and imaging

Mice were sacrificed ~4 weeks after injection and the whole, intact lung was immediately extracted and imaged. A tube was inserted into the trachea and secured by tying a suture around the trachea. The tube was used to inflated the lung with PBS. The pleural surface of the lung was imaged with 2-photon microscopy or confocal microscopy to identify metastatic nodules and PA beads at the surface of the lung.

In vitro and multi-modal intravital imaging

Imaging with fluorescent stereomicroscope

The Royal Blue SFA Stereo Microscope Fluorescence Adapter (NIGHTSEA) was used with a stereomicroscope to visualize tumors above 1mm in diameter.

Confocal imaging for in vitro measurements of solid stress in tumor spheroids

In vitro spheroid images were acquired using the Olympus FV3000 laser scanning confocal microscope using either a UPLSAPO10X2 (Olympus, NA 0.4, 10x magnification) or LUCPLFLN20X (Olympus, NA 0.45, 20x magnification) air immersion objective lens (Olympus) at scanning resolutions between 512x512 and 1024x1024 pixels. MCa-M3C-H2B-dendra2 cells were imaged using a 488nm laser excitation and a 525/60 nm variable barrier filter. Rhodamine-labelled polyacrylamide beads were imaged using a 561nm laser excitation and a 600/50 variable barrier filter (Olympus).

Intravital imaging

Tumors were size-matched for measuring solid stress at the cellular- and tissue-scales. Inhalation of isoflurane (1.5-2% vol/vol, 0.1-0.5L/min, Kent Scientific 0-1 LPM VetFlo system) was used to anesthetize the animal during imaging. An intravital mammary window was implanted for 2-photon or OCT imaging and the intravital window was immobilized by an in-house fabricated stage (Fig. S1). 2-photon imaging was used for imaging cellular-scale PA beads, and OCT was used to image tissue-scale PA beads. The glass coverslip on the intravital window was removed for imaging when tumors were formed prior to window implantation to prevent artificial compression of the tumor during imaging. Imaging was performed approximately 5-7 days after cancer cell injection, unless otherwise noted.

Two-photon (2P) microscopy system

2P images were taken with a 16x water immersion objective lens (16X Nikon CFI LWD Plan Fluorite Objective, 0.08 NA) using the Bruker Investigator system, which consists of an Insight X3 laser (Spectra Physics). The system has a 700 nm short-pass primary dichroic with an IR blocker (Chroma) in the detection path. A filter cube with 595/50 nm and 525/70 nm filters (Chroma) and a 565 nm long-pass secondary dichroic (Chroma) were used to image fluorescently-labelled cells and beads and lung autofluorescence. Samples were excited with 880 nm using a laser power of approximately 50 mW at the sample plane. Images were taken at scanning resolutions between 512x512 to 1024x1024 pixels with 1-3x digital zoom using galvo scanning without averaging. PrairieView software (Bruker) was used for 2P imaging.

Optical coherence tomography system

We used a commercial spectral-domain OCT system (Telesto TEL320C1, Thorlabs, New Jersey). The light source is a broadband superluminescent diode with center wavelength of 1300 nm and a full width half maximum bandwidth of 150 nm, yielding an axial resolution of 4.2 µm in tissue. The spectrometer has a 2048-pixel InGaAs line scan camera operating at an A-line rate of 76 kHz. The total imaging depth is 2.6 mm in tissue. A 10× air objective (Mitutoyo, 0.28 NA) was used in the sample arm, which yields a lateral resolution of 3.5 µm with a theoretical Rayleigh range of 40 µm in a nonscattering medium. The maximum sensitivity of the system is 109 dB.

Euthanasia

Euthanasia was performed by intraperitoneal (IP) injecting 150mg/kg of Euthasol (Virbac).

Collagenase/hyaluronidase treatment for tumor dissociation

Collagenase/hyaluronidase enzyme solution was prepared by dissolving 100mg collagenase from *Clostridium histolyticum* (Sigma, C0130), 50mg hyaluronidase from bovine testes (Sigma, H3506), and 2mg $CaCl_2$ in 30 mL DMEM. The coverslip from the intravital window was removed and we applied the enzyme solution to animals post-euthanasia to comply with our animal protocols. For tissue-scale experiments, the enzyme solution was applied to the tumor without excision and incubated at 37 °C for 180 minutes using a thermostatic heating pad. For cellular-scale experiments, tumors were excised and placed in the enzyme solution at 37 °C.

Trypsin treatment for spheroid dissociation

The media from individual wells of spheroids cultured in 96-well plates was removed and the spheroids were washed twice with PBS in the wells to remove serum proteins. Trypsin-EDTA (0.05%) (Gibco) was added to each spheroid in the 96-well plate and the spheroids were incubated for 24 hours at 37 °C to fully dissociate the cells.

Histology of tumor sections

Tumors were resected and fixed with 4% paraformaldehyde overnight and cryoprotected with 15% sucrose, followed by 30% sucrose. The tumors were embedded in optimal temperature cutting compound, flash frozen, and cryosectioned into 10 µm slices. Tissue sections were stained with hematoxylin and eosin. Slides were imaged using the Olympus VS120 Virtual Slide Scanner.

Quantification of solid stress

Image segmentation of 3-D confocal, two-photon, and OCT image stacks

An edge detection algorithm was written in MATLAB (Mathworks) to segment out cellular-scale polyacrylamide bead 3-D image stacks taken by confocal or two-photon microscopy. Tissue-scale 3-D image stacks taken by OCT were manually segmented in MATLAB (Mathworks) using the drawfreehand function (Fig. S13).

3-D ellipsoid fitting

After image segmentation, the 3-D ellipsoid fitting program cropped the 3D image file to a user-defined 3D region of interest around the microsphere. As our images typically had a factor of 10 higher resolution in the x- and y-dimensions than in the z-dimension, the image was then up-sampled in the z-dimension by a factor of *x,y resolution / z resolution*. Ray tracing originating at the geometric centroid of the image determined the intensity profiles along a set of rays iterating through all values for ϕ and Θ of the polar coordinate axes. Intensity profiles were then fit to a sigmoid of the form

$$a + ((b + c(x - d))/(1 + exp(e * (x - d))))$$

where *x* is the distance radially outward from the geometric centroid of the image stack. Variable parameters *a, b, c, d,* and *e* for ray profiles were optimized through least squares fitting using the

Levenberg-Marquardt algorithm. Intensity profiles that could not be fit by linear least squares were discarded, but were at a low enough occurrence they did not affect the overall resolution of the point cloud approximation. The boundary of the microsphere was estimated to lie at where the sigmoid function reached 50% of its maximum intensity. To prevent over-fitting of the ellipsoid, boundary points were down-sampled first as a function of ϕ (ϕ = 5:25, 155:180, reduction in points by 6x; ϕ = 30:50, 130:150, reduction in points by 4x; ϕ = 55:125, reduction in points by 2x) and then in total by a further 40%, so that 60% of the points are used in the downstream fitting process: in the creation of the analysis pipeline, 10 simulations were run for down-sampling values from 10% to 90% in increments of 10%. When the residual distance between each boundary point and the closest face of the ellipsoid was calculated and normalized by the total number of points used in that fit, a 40% reduction showed the best balance between fit accuracy and variability. Down-sampled point clouds were fit to an affine invariant 3D ellipsoid using a Douglas-Rachford iterative algorithm with singular value[62]. Ellipsoid diameters and centers were calculated from the modeled 3D surface map. Visualization of the process can be found in Figure S13.

Aspect ratio measurement

The ratio of the largest to smallest axis length of the ellipsoid fit was taken as the aspect ratio of the polyacrylamide bead.

Elastic energy density

To calculate elastic energy density, the original, undeformed bead diameters are needed. To obtain the original bead state, the tissue or spheroid is enzymatically dissociated, as described in methods above. However, in cases in which the tissue or spheroid is not dissociated, we estimated the original undeformed diameter to be the length of the largest diameter of the deformed bead (Fig. S6). The undeformed and deformed bead centroids were centered and an in-house MATLAB script was used determine the deformation field required to deform the polyacrylamide bead from the undeformed to deformed state using the minimum amount of surface strain energy.

Mathematical modeling

An axisymmetric finite-element code was developed in ABAQUS (Dassault Systèmes) to translate the stress-induced deformation to solid stress. We used element type C3D10, a quadratic axisymmetric tetrahedral element to mesh the undeformed and deformed bead in ABAQUS. We defined a hyperelastic material, with test stress/strain data from the indentation of a polyacrylamide gel, obtained using an Instron 5900 Series System. The test data was fit using Ogden 3rd order hyperelastic model in ABAQUS, with a Poisson's ratio of 0.22. A linear stress/strain curve representing constant Young's modulus was fit to the first point of the nonlinear stress/strain curve (Fig. S3). The slope of the linear stress/strain curve was determined by average Young's modulus values of cellular- and tissue-scale beads, obtained via AFM. The undeformed bead diameter was estimated as the longest axis length of the deformed bead. The centroids of the deformed and undeformed beads were aligned (ellipsoid estimation) or the location of the centroid of the deformed relative to the centroid of the undeformed bead was determined by finding the lowest surface strain energy (actual deformed geometry) to determine the boundary conditions, which were set as the deformation of the individual nodes from the

undeformed to the deformed state. Based on the deformation field, the maximum solid stress was determined, in addition to the total elastic energy density required to deform the bead using a quasi-static condition with non-linear geometry enabled. The elastic energy density is given by the function,

$$Elastic\ energy\ density\ (W) = \frac{1}{2V}\int_V \sigma_{ij}\varepsilon_{ij}dV$$

where σ_{ij} is the stress tensor, ε_{ij} is the strain tensor, and *V* is the volume of the microsphere. The absolute maximum principal stresses and average maximum principal stress are reported. Poisson's ratio was measured to be 0.22 ± 0.028, and Young's modulus was separately determined by AFM (taken as the average) for the cellular scale (215 Pa) and for the tissue scale (383 Pa). The density of the polyacrylamide bead was assumed to be 1.3 g/cm^3.

AFM-based measurement of indentation modulus

The indentation moduli of polyacrylamide beads, single cells, spheroids and tumor samples were quantified using an Asylum MFP3D atomic force microscope (Asylum Research, Santa Barbara, CA). Polyacrylamide beads were immobilized on plasma-treated glass slides. Spheroids were immobilized on Cell-Tak treated glass slides. Cells were grown on glass coverslips. Tumors were resected, cut in half, and immobilized on glass slides using cyanoacrylate glue. We used polystyrene colloidal probe tips with end radius R ~ 15 µm (Polysciences, Warrington, PA) attached to tipless cantilevers with nominal spring constant k ~ 0.2 N/m (Bruker, Camarillo, CA). The colloidal probes were attached to the cantilever by the following process: a dot of glue (Hernon Ultrabond 721) was applied onto a tipless cantilever by making quick contact between the cantilever and a thin layer of glue (1 µl) spread over a glass surface and then immediate contact was made between the tip of the cantilever and a colloid probe resting on a glass slide for 1 min with the cantilever pushing against the colloid. This process was followed by UV curing for 30 seconds. For each probe tip, the exact spring constants of the cantilevers were directly measured using the thermal calibration method[63]. The relationship between the detected voltage and the applied force was calibrated by bringing the cantilever in contact with a glass slide and calculating the slope of the voltage-displacement curve. The displacement, d, was translated to force, F, using Hooke's Law (F = kd). The indentation was performed under a force control scheme (max force ~20nN), limiting the indentation depths to 0.5–3 µm. The tip displacement was obtained by subtracting the cantilever deflection from vertical movement of the piezo. An indentation approach velocity of 2 µm/s ensured probing the elastic modulus at a lower rate, close to equilibrium condition.

The effective indentation modulus E_{ind} was computed using Hertzian contact mechanics models via least-squares linear regression of the experimental loading force-displacement curves. For the spherical colloidal probe tip with end radius R_1 on the sample with thickness R_2 (here, R_2 ~ 50-500 µm, R_1~ 15 µm),

$$F = \frac{4}{3}E_{ind}\left(\frac{R_1R_2}{R_1+R_2}\right)^{\frac{1}{2}} * \frac{(d_{total})^{\frac{3}{2}}}{1+\left(\frac{R_1}{R_1+R_2}\right)^{\frac{1}{3}}}$$

where F is the indentation force and d_{total} is the indentation depth.

For tumor samples which have much higher R_2 compared to the colloidal probe tip radius R_1, the force equation simplifies to

$$F = \frac{2}{3} E_{ind} * (d_{total})^{\frac{3}{2}}$$

A modified Hertz model for bonded, thin samples was used to calculate the E_{ind} in single cells[64]:

$$F = \frac{16E_{ind}}{9} R^{\frac{1}{2}} (d_{total})^{\frac{3}{2}} * [1 + 1.133\chi + 1.283\chi^2 + 0.769\chi^3 + 0.0975\chi^4]$$

$$\chi = \sqrt{\frac{R * d_{total}}{h}}$$

where R is the radius of the colloidal probe tip (R=20μm) and h is the height of the cell (h=8μm).

Statistical analysis

Groups were compared using an unpaired, two-sided Student's t-test (due to independent sampling) or one-way ANOVA followed by Tukey's multiple comparisons test. Paired statistics were not performed since the same polyacrylamide beads could not always be tracked longitudinally.

References:

1. Nia HT, Munn LL, Jain RK. Physical traits of cancer. *Science (80-)*. 2020;370(6516):1-9. doi:10.1126/science.aaz0868

2. Kechagia JZ, Ivaska J, Roca-Cusachs P. Integrins as biomechanical sensors of the microenvironment. *Nat Rev Mol Cell Biol*. 2019;20(8):457-473. doi:10.1038/s41580-019-0134-2

3. Benham-Pyle BW, Pruitt BL, Nelson WJ. Mechanical strain induces E-cadherin-dependent Yap1 and β-catenin activation to drive cell cycle entry. *Science (80-)*. 2015;348(6238):1024-1027. doi:10.1126/science.aaa4559

4. Munn LL, Nia HT. *Mechanosensing Tensile Solid Stresses*. Vol 116. National Academy of Sciences; 2019:21960-21962. www.pnas.org/cgi/doi/10.1073/pnas.1916115116. Accessed June 30, 2021.

5. Levayer R. Solid stress, competition for space and cancer: The opposing roles of mechanical cell competition in tumour initiation and growth. *Semin Cancer Biol*. 2019;63:69-80. doi:10.1016/j.semcancer.2019.05.004

6. Smith ML, Gourdon D, Little WC, et al. Force-induced unfolding of fibronectin in the extracellular matrix of living cells. *PLoS Biol*. 2007;5(10):2243-2254. doi:10.1371/journal.pbio.0050268

7. Saini K, Cho S, Dooling LJ, Discher DE. Tension in fibrils suppresses their enzymatic degradation – A molecular mechanism for 'use it or lose it.' *Matrix Biol*. 2020;85-86:34-46. doi:10.1016/j.matbio.2019.06.001

8. Kubow KE, Vukmirovic R, Zhe L, et al. Mechanical forces regulate the interactions of fibronectin and collagen i in extracellular matrix. *Nat Commun*. 2015;6:8026. doi:10.1038/ncomms9026

9. Kirby TJ, Lammerding J. Emerging views of the nucleus as a cellular mechanosensor. *Nat Cell Biol*. 2018;20(4):373-381. doi:10.1038/s41556-018-0038-y

10. Cho S, Irianto J, Discher DE. Mechanosensing by the nucleus: From pathways to scaling relationships. *J Cell Biol*. 2017;216(2):305-315. doi:10.1083/jcb.201610042

11. Chauhan VP, Martin JD, Liu H, et al. Angiotensin inhibition enhances drug delivery and potentiates chemotherapy by decompressing tumour blood vessels. *Nat Commun*. 2013;4(1). doi:10.1038/ncomms3516

12. Padera TP, Stoll BR, Tooredman JB, Capen D, Di Tomaso E, Jain RK. Cancer cells compress intratumour vessels. *Nature*. 2004;427(6976):695. doi:10.1038/427695a

13. Stylianopoulos T, Martin JD, Chauhan VP, et al. Causes, consequences, and remedies for growth-induced solid stress in murine and human tumors. *Proc Natl Acad Sci U S A*. 2012;109(38):15101-15108. doi:10.1073/pnas.1213353109

14. Jain RK. Antiangiogenesis Strategies Revisited: From Starving Tumors to Alleviating Hypoxia. *Cancer Cell*. 2014;26(5):605-622. doi:10.1016/j.ccell.2014.10.006

15. Munn LL, Jain RK. Vascular regulation of antitumor immunity. *Science (80-)*. 2019;365(6453):544-545. doi:10.1126/science.aaw7875

16. Jones D, Wang Z, Chen IX, et al. Solid stress impairs lymphocyte infiltration into lymph-node metastases. *Nat Biomed Eng 2021 512*. 2021;5(12):1426-1436. doi:10.1038/s41551-021-00766-1

17. Tse JM, Cheng G, Tyrrell JA, et al. Mechanical compression drives cancer cells toward invasive phenotype. *Proc Natl Acad Sci U S A*. 2012;109(3):911-916. doi:10.1073/pnas.1118910109

18. Das J, Maiti TK. Mechanical Stress-Induced Autophagy: A Key Player in Cancer Metastasis. In: *Autophagy in Tumor and Tumor Microenvironment*. ; 2020:171-182. doi:10.1007/978-981-15-6930-2_8

19. Fernández-Sánchez ME, Barbier S, Whitehead J, et al. Mechanical induction of the tumorigenic β-catenin pathway by tumour growth pressure. *Nature*. 2015;523(7558):92-95. doi:10.1038/nature14329

20. Seano G, Nia HT, Emblem KE, et al. Solid stress in brain tumours causes neuronal loss and neurological dysfunction and can be reversed by lithium. *Nat Biomed Eng*. 2019;3(3):230-245. doi:10.1038/s41551-018-0334-7

21. Nia HT, Datta M, Seano G, et al. In vivo compression and imaging in mouse brain to measure the effects of solid stress. *Nat Protoc*. 2020;15(8):2321-2340. doi:10.1038/S41596-020-0328-2

22. Provenzano PP, Cuevas C, Chang AE, Goel VK, Von Hoff DD, Hingorani SR. Enzymatic Targeting of the Stroma Ablates Physical Barriers to Treatment of Pancreatic Ductal Adenocarcinoma. *Cancer Cell*. 2012;21(3):418-429. doi:10.1016/j.ccr.2012.01.007

23. Zhao Y, Cao J, Melamed A, et al. Losartan treatment enhances chemotherapy efficacy and reduces ascites in ovarian cancer models by normalizing the tumor stroma. *Proc Natl Acad Sci U S A*. 2019;116(6):2210-2219. doi:10.1073/pnas.1818357116

24. *ClinicalTrials.Gov: Proton w/FOLFIRINOX-Losartan for Pancreatic Cancer; Identifier NCT01821729.*

25. Murphy JE, Wo JY, Ryan DP, et al. Total Neoadjuvant Therapy with FOLFIRINOX in Combination with Losartan Followed by Chemoradiotherapy for Locally Advanced Pancreatic Cancer: A Phase 2 Clinical Trial. *JAMA Oncol*. 2019. doi:10.1001/jamaoncol.2019.0892

26. Nia HT, Liu H, Seano G, et al. Solid stress and elastic energy as measures of tumour mechanopathology. *Nat Biomed Eng*. 2017;1(1). doi:10.1038/s41551-016-0004

27. Nia HT, Datta M, Seano G, Huang P, Munn LL, Jain RK. Quantifying solid stress and elastic energy from excised or in situ tumors. *Nat Protoc*. 2018;13(5):1091-1105. doi:10.1038/nprot.2018.020

28. Lee W, Kalashnikov N, Mok S, et al. Dispersible hydrogel force sensors reveal patterns of solid mechanical stress in multicellular spheroid cultures. *Nat Commun*. 2019;10(1):1-14. doi:10.1038/s41467-018-07967-4

29. Dolega ME, Delarue M, Ingremeau F, Prost J, Delon A, Cappello G. Cell-like pressure sensors reveal increase of mechanical stress towards the core of multicellular spheroids under compression. *Nat Commun*. 2017;8. doi:10.1038/ncomms14056

30. Mohagheghian E, Luo J, Chen J, et al. Quantifying compressive forces between living cell layers and within tissues using elastic round microgels. *Nat Commun*. 2018;9(1):1-14. doi:10.1038/s41467-018-04245-1

31. Girardo S, Träber N, Wagner K, et al. Standardized microgel beads as elastic cell mechanical probes. *J Mater Chem B*. 2018;6(39):6245-6261. doi:10.1039/C8TB01421C

32. Takao S, Taya M, Chiew C. Mechanical stress-induced cell death in breast cancer cells. *Biol Open*.

2019;8(8). doi:10.1242/BIO.043133

33. Matamoro-Vidal A, Levayer R. Multiple Influences of Mechanical Forces on Cell Competition. *Curr Biol*. 2019;29(15):R762-R774. doi:10.1016/J.CUB.2019.06.030

34. Wagstaff L, Goschorska M, Kozyrska K, et al. Mechanical cell competition kills cells via induction of lethal p53 levels. *Nat Commun*. 2016;7(1):1-14. doi:10.1038/ncomms11373

35. Shah MK, Leary EA, Darling EM. Integration of hyper-compliant microparticles into a 3D melanoma tumor model. *J Biomech*. 2019;82:46-53. doi:10.1016/j.jbiomech.2018.10.018

36. Li W, Li S, Chen IX, et al. Combining losartan with radiotherapy increases tumor control and inhibits lung metastases from a HER2/neu-positive orthotopic breast cancer model. 2021;16(1):1-12. https://ro-journal.biomedcentral.com/articles/10.1186/s13014-021-01775-9. Accessed July 9, 2021.

37. Gross B, Shelton E, Gomez C, Campàs O. STRESS, an automated geometrical characterization of deformable particles for in vivo measurements of cell and tissue mechanical stresses. *bioRxiv*. March 2021:2021.03.26.437148. doi:10.1101/2021.03.26.437148

38. Stylianopoulos T, Jain RK. Combining two strategies to improve perfusion and drug delivery in solid tumors. *Proc Natl Acad Sci U S A*. 2013;110(46):18632-18637. doi:10.1073/PNAS.1318415110/SUPPL_FILE/PNAS.201318415SI.PDF

39. Jacobetz MA, Chan DS, Neesse A, et al. Hyaluronan impairs vascular function and drug delivery in a mouse model of pancreatic cancer. *Gut*. 2013;62(1):112-120. doi:10.1136/GUTJNL-2012-302529

40. Chauhan VP, Boucher Y, Ferrone CR, et al. Compression of Pancreatic Tumor Blood Vessels by Hyaluronan Is Caused by Solid Stress and Not Interstitial Fluid Pressure. *Cancer Cell*. 2014;26(1):14-15. doi:10.1016/j.ccr.2014.06.003

41. DelGiorno KE, Carlson MA, Osgood R, et al. Interstitial pressure and vascular collapse in pancreas cancer:fluids and solids, measurement and meaning. *Cancer Cell*. 2014;26(1):16. doi:10.1016/J.CCR.2014.06.004

42. Boucher Y, Baxter LT, Jain4 RK. Interstitial Pressure Gradients in Tissue-isolated and Subcutaneous Tumors: Implications for Therapy1. *CANCER Res*. 1990;50:4478-4484.

43. Zanetti-Dällenbach R, Plodinec M, Oertle P, et al. Length scale matters: Real-time elastography versus nanomechanical profiling by atomic force microscopy for the diagnosis of breast lesions. *Biomed Res Int*. 2018;2018. doi:10.1155/2018/3840597

44. Plodinec M, Loparic M, Monnier CA, et al. The nanomechanical signature of breast cancer. *Nat Nanotechnol*. 2012;7(11):757-765. doi:10.1038/NNANO.2012.167

45. Vinci M, Gowan S, Boxall F, et al. Advances in establishment and analysis of three-dimensional tumor spheroid-based functional assays for target validation and drug evaluation. *BMC Biol*. 2012;10(1):1-21. doi:10.1186/1741-7007-10-29/FIGURES/8

46. Padera TP, Kuo AH, Hoshida T, et al. Differential response of primary tumor versus lymphatic metastasis to VEGFR-2 and VEGFR-3 kinase inhibitors cediranib and vandetanib. *Mol Cancer Ther*. 2008;7(8):2272-2279. doi:10.1158/1535-7163.MCT-08-0182

47. Solis AG, Bielecki P, Steach HR, et al. Mechanosensation of cyclical force by PIEZO1 is essential for innate immunity. *Nature*. 2019;573(7772):69-74. doi:10.1038/S41586-019-1485-8

48. Maruyama K, Nemoto E, Yamada S. Mechanical regulation of macrophage function - Cyclic tensile force inhibits NLRP3 inflammasome-dependent IL-1β secretion in murine macrophages. *Inflamm Regen*. 2019;39(1):1-9. doi:10.1186/S41232-019-0092-2/FIGURES/5

49. Li C, Hu Y, Mayr M, Xu Q. Cyclic Strain Stress-induced Mitogen-activated Protein Kinase (MAPK) Phosphatase 1 Expression in Vascular Smooth Muscle Cells Is Regulated by Ras/Rac-MAPK Pathways. *J Biol Chem*. 1999;274(36):25273-25280. doi:10.1074/JBC.274.36.25273

50. Chauhan VP, Chen IX, Tong R, et al. Reprogramming the microenvironment with tumorselective angiotensin blockers enhances cancer immunotherapy. *Proc Natl Acad Sci U S A*. 2019;166(22):10674-10680. doi:10.1073/pnas.1819889116

51. Martin JD, Seano G, Jain RK. Normalizing Function of Tumor Vessels: Progress, Opportunities, and Challenges. *Annu Rev Pathol*. 2019;81(505). doi:10.1146/annurev-physiol-020518

52. Cleaver O, Melton DA. Endothelial signaling during development. *Nat Med 2003 96*. 2003;9(6):661-668. doi:10.1038/nm0603-661

53. Jain RK. Normalization of tumor vasculature: An emerging concept in antiangiogenic therapy. *Science (80-)*. 2005;307(5706):58-62. doi:10.1126/science.1104819

54. Jain RK. Normalizing tumor microenvironment to treat cancer: Bench to bedside to biomarkers. In: *Journal of Clinical Oncology*. Vol 31. American Society of Clinical Oncology; 2013:2205-2218. doi:10.1200/JCO.2012.46.3653

55. Stylianopoulos T, Munn LL, Jain RK. Reengineering the Physical Microenvironment of Tumors to Improve Drug Delivery and Efficacy: From Mathematical Modeling to Bench to Bedside. *Trends in Cancer*. 2018;4(4). doi:10.1016/j.trecan.2018.02.005

56. Nava MM, Miroshnikova YA, Biggs LC, et al. Heterochromatin-Driven Nuclear Softening Protects the Genome against Mechanical Stress-Induced Damage. *Cell*. 2020;181(4):800-817.e22. doi:10.1016/J.CELL.2020.03.052

57. Wirtz D, Konstantopoulos K, Searson PC. *The Physics of Cancer: The Role of Physical Interactions and Mechanical Forces in Metastasis*. Vol 11. Nat Rev Cancer; 2011:512-522. doi:10.1038/nrc3080

58. Lefrançais E, Ortiz-Muñoz G, Caudrillier A, et al. The lung is a site of platelet biogenesis and a reservoir for haematopoietic progenitors. *Nat 2017 5447648*. 2017;544(7648):105-109. doi:10.1038/nature21706

59. Johnston I, Hayes V, Poncz M. Threading an elephant through the eye of a needle: Where are platelets made? *Cell Res 2017 279*. 2017;27(9):1079-1080. doi:10.1038/cr.2017.65

60. Tse JR, Engler AJ. Preparation of hydrogel substrates with tunable mechanical properties. *Curr Protoc Cell Biol*. 2010;(SUPPL. 47):1-16. doi:10.1002/0471143030.cb1016s47

61. Chen IX, Chauhan VP, Posada J, et al. Blocking CXCR4 alleviates desmoplasia, increases T-lymphocyte infiltration, and improves immunotherapy in metastatic breast cancer. *Proc Natl Acad Sci U S A*. 2019;116(10):4558-4566. doi:10.1073/pnas.1815515116

62. Kovac B, Fehrenbach J, Guillaume L, Weiss P. FitEllipsoid: a fast supervised ellipsoid segmentation plugin. *BMC Bioinformatics*. 2019;20(142). doi:10.1186/s12859-019-2673-0

63. Hutter JL, Bechhoefer J. Calibration of atomic-force microscope tips. *Rev Sci Instrum*. 1998;64(7):1868. doi:10.1063/1.1143970

64. Dimitriadis EK, Horkay F, Maresca J, Kachar B, Chadwick RS. Determination of Elastic Moduli of Thin Layers of Soft Material Using the Atomic Force Microscope. *Biophys J*. 2002;82(5):2798-2810. doi:10.1016/S0006-3495(02)75620-8

Acknowledgments

We thank Neurophotonics Center at Boston University for their generous support and access to their facility. This work was supported by R21EB031332, and seed funds from Center for Multiscale and Translational Mechanobiology, and American Cancer Society Institutional Fund at Boston University.

Research reported in this publication was supported by the Boston University Micro and Nano Imaging Facility and the Office of the Director, National Institutes of Health of the National Institutes of Health under award Number S10OD024993. The content is solely the responsibility of the authors and does not necessarily represent the official views of the National Institute of Health.

Supplementary Files

This is a list of supplementary files associated with this preprint. Click to download.

- SupplementaryFiguresfinalsolidstress.pdf